Utilization of 3D printed carbon gas diffusion layers in polymer electrolyte membrane fuel cells

Utilization of 3D printed carbon gas diffusion layers in polymer electrolyte membrane fuel cells

Daniel Niblett [a,1,*], *Zunmin Guo* [b,1], *Stuart Holmes* [b], *Vahid Niasar* [b], *Robert Prosser* [a]

[a] *Department of Mechanical, Aerospace and Civil Engineering, University of Manchester, Manchester, M13 9LP, UK*
[b] *Department of Chemical Engineering, University of Manchester, Manchester, M13 9LP, UK*

HIGHLIGHTS

- A designed carbon gas diffusion layer is manufactured using 3D printing.
- Controlled pyrolysis is used to preserve microstructure.
- Challenges for 3D printed materials integrated into fuel cells are highlighted.
- Simulations show an 8% higher oxygen concentration at the catalyst layer.

GRAPHICAL ABSTRACT
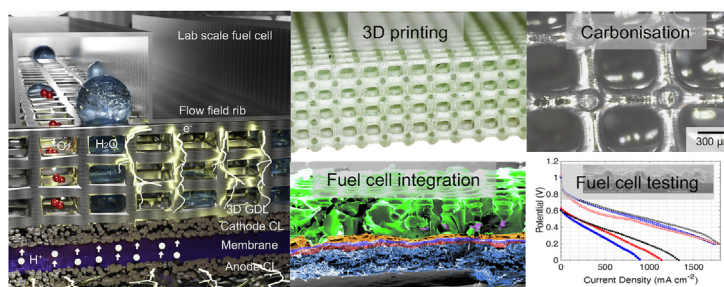
ARTICLE INFO

ABSTRACT

3D printing and carbonisation is used to produce designed gas diffusion layer materials for polymer electrolyte membrane fuel cells (PEMFC). Using a desktop UV 3D printer, designed porous microstructures are printed with micro and macro-scale features. Successful improvement of the pyrolysis process maintains the structural accuracy during carbonisation, reducing the material to electrically conductive carbon. The size of the material allows for testing in a lab scale fuel cell with 1.5×1.5 cm electrode size, which shows lower but interesting electrochemical performance (power density of 205 mW cm^{-2}). Challenges associated with integration of a 3D printed structure into a membrane electrode assembly are highlighted, including the low open circuit voltage caused by large amounts of membrane deformation and subsequent hydrogen crossover. This study shows that it is possible to design and manufacture a gas diffusion layer for fuel cells. Numerical simulation on the new GDL structure shows that advective-diffusive transport of oxygen in the 3D printed design is superior to conventional carbon paper. This study serves as the first attempt to implement 3D printed microstructures as GDL into PEMFC.

---

* *Corresponding author.*
E-mail address: daniel.niblett@manchester.ac.uk (D. Niblett).
[1] Daniel Niblett and Zunmin Guo contributed equally to this paper.

Introduction

Polymer electrolyte membrane fuel cells (PEMFCs) are useful devices for converting energy stored as hydrogen to electrical energy with no harmful emissions. This is especially important for hard to de-carbonise transportation solutions [1]. To increase the uptake of fuel cells in commercial applications, research into improving the efficiency and durability of PEMFC are ongoing. PEMFC, hydrogen and oxygen are combined electrochemically in a porous system separated by a polymer membrane [2] where water is produced at the cathode catalyst layer. The water produced competes for the same space as the supplying reactant air, blocking the space for oxygen transport. At the same time, electrons travel through the solid carbon structure to complete the reaction. The system of processes is depicted in Fig. 1 (a). The transport of oxygen and water in this system is not straight-forward; water can accumulate in the porous network due to the strength of the capillary forces and droplet removal in the air supply channels is periodic [3]. Efficient removal of water, as well as optimal oxygen transport to the catalyst layer is essential to reduce resistances [4].

It has been shown that different gas diffusion layers can effect the performance and limiting current density of the cell [5]. Therefore, changes to the porous structure, designed to address optimal water and oxygen transport should also reduce mass transport losses. Water and oxygen distribution in the cell is also determined by the flow field design, which can cause additional convection especially in the under rib regions [6] and by the presence of water in the channels [3].

Fractures can be present in the microporous layer applied to GDL materials. Although, while these can be beneficial to water management [3], it has been shown that reducing the number of cracks can be beneficial improving interface contact area [7]. By using a GDL with an ordered design, effective transport properties of permeability, diffusivity and water management could be improved, with the focus on cubic lattices with anisotropy in the in-plane direction [8,9].

Other methods to change the GDL porous structure have been attempted using both exploratory simulations and experiments with new materials [10]. A woven fabric based GDL design has shown improvements to performance, where larger pores are clear for oxygen transport and water to be removed wicks around the hydrophilic fibres [11]. Modifications to GDL wettability have led to greater performance at high current density, due to tailoring water into hydrophilic pathways [12]. Additionally, a 3D printing method has been used to prepare a titanium based structure without microstructure control, which resulted in a lower performance than the carbon paper design [13]. In a simulation study considering simultaneous oxygen transport through the GDL and water two-phase flow, it was shown that a non-uniform porosity gradient can increase the current density due to a reduction in the water accumulation [14].

Electrospun materials offer an alternative to traditional carbon paper GDL [15], are also very suitable for low temperature fuel cell systems. These materials offer a smaller pore and fibre diameter (<2 μm) [16] compared to traditional carbon paper (9 μm) [8] and have been used as flexible Li-ion
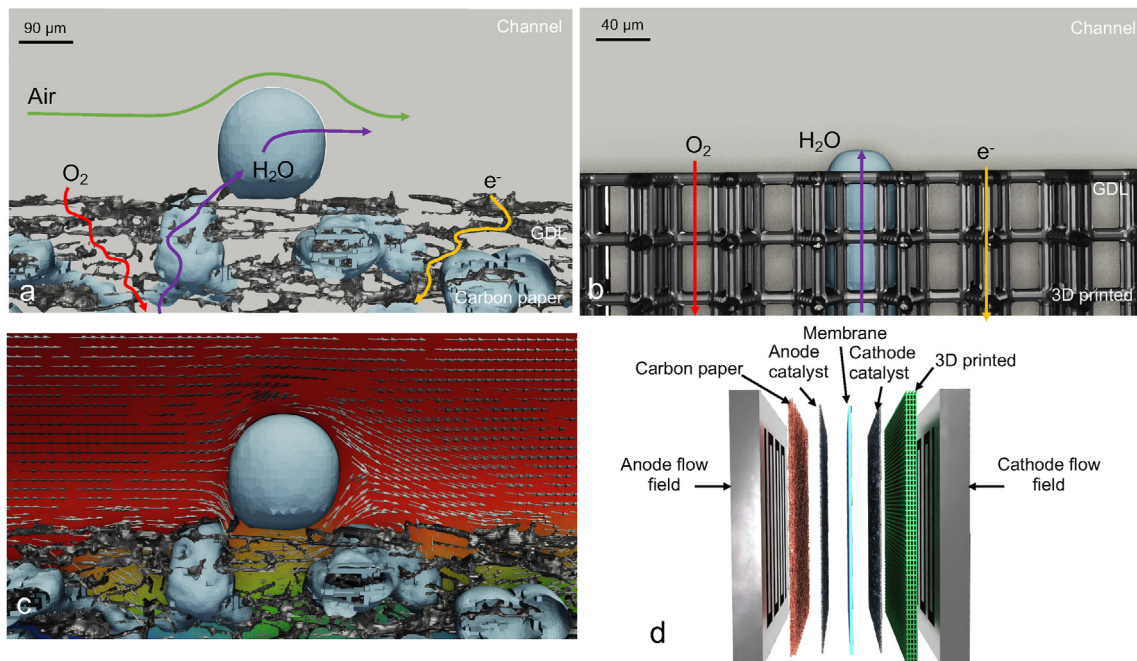
Fig. 1 − **Schematics of processes occurring in an operating fuel cell gas diffusion layer and channel for: (a) conventional carbon paper material and (b) 3D printed carbon material. Oxygen diffuses (red) and water percolates (purple) through the pore space. Oxygen is supplied and water is removed by the air flow in the channel (green) and electrons are transported in the carbon structure (yellow). (c) shows the oxygen concentration gradient and velocity vectors for flow and transport in this system. (d) shows the replacement of the cathode GDL with 3D printed material used in this study. (For interpretation of the references to color in this figure legend, the reader is referred to the Web version of this article.)**

battery electrodes [17], Anion exchange membrane fuel cell catalysts [18] and redox flow battery electrodes [16]. After manufacturing, these materials must also be carbonised between 800 and 1000 °C using nitrogen.

The carbon paper based GDL used in PEMFC can degrade in performance over time. The material structure can become weakened through carbon corrosion, with binder and PTFE being removed [19]. To address both the mass transport issues and potential durability challenges, a 3D printed design does not use binder and can handle higher compression stress [20] leading to a higher durability. Modifications to GDL wettability may also impact its connection with the channel; hydrophilic modifications to the GDL impact the available mass transfer area from the channels if a film is developed on the GDL-channel interface [3].

There is a balance between the optimal hydrophobic coating amount and distribution required by the GDL for effective water removal. An excessive amount can hinder oxygen mass transport [21] and cause higher electron transfer resistance [22]. A GDL with a patterned wettability can have variable performance when the pattern is aligned differently with the hydrophilic flow field rib and channels. This indicates that water accumulation under the rib and channel are both important to consider when altering the wettability of GDL [23]. Furthermore, X-ray imaging has been used to study the coating effect (from 0 to 60% coating) on the distribution of contact angles inside the GDL. There was a marked increase in advancing and receding contact angle between 0 and 10%, with the intrinsic GDL contact angle being more hydrophilic than the measured external surface droplet measurement [24].

Optimisation of both the properties of the flow field and the channel are required to reach the highest oxygen concentration across the cell [25]. Using a 3D printed titanium flow field and GDL, water can be moved through the hydrophilic backbone, and make use of the space within the solid rib regions to remove water, which can lead to an improved performance at high current density [26]. Using designed structures, the thickness of the GDL can be tuned, which will have an impact on the water management and mass transport capability of the material [27].

Additive manufacturing methods (3D printing) offer an alternative to material manufacture, producing pores-scale structures that are specifically designed for the processes that they handle [8]. The simplification of the gas diffusion layer into a structured system is shown in Fig. 1 (b), which highlights the improvement to oxygen, water and electron transport that could be possible. Fig. 1 (c) shows the interaction between the flow in the channels and flow in the gas diffusion layer where the oxygen transport (colour gradient) occurs in the space surrounding the removal of water. Performing coupled simulations of these competing phenomena provides a means of exploring the potential improvements that could be obtained through a structured GDL design [9].

3D printed materials have been used in other applications to great success. In microbial fuel cells, a 3D printed carbon electrode achieved a higher power density than carbon paper due to the former's increased surface area, mass transport and high bio-compatibility [28]. In the same application, UV cured polymer microstructures have been coated with copper achieving 8 times higher power density than copper mesh electrodes [29], highlighting the importance of reactant mass transport through microstructure design. In redox flow batteries (RFB), the carbon paper electrodes are also not ideal due to low surface area and variability in pore size [30]. It was shown that microstructures with a gradient in porosity would reduce the mass transport resistances [30]. 3D carbon electrodes used in Li-ion batteries offer higher performance for energy storage (Li-ion) with lower tortuosity (effective reactant diffusivity) and have good mechanical strength [31]. In general, microstructure lattices can provide the means to optimising pathways and surface area for gas absorption and water movement [32].

Compression of the GDL can damage the porous microstructure [33], which could cause problems with oxygen and water distribution [34], as well as potential membrane damage, leading to hydrogen crossover [35]. A designed lattice structure can be designed to resist the compressionspecifically iso-truss or oct-truss designs as shown in Ref. [36] offer the highest Young's modulus and compression strength, reaching close to the theoretical limit of carbon materials [20,37].

Advanced ceramic materials present in solid oxide fuel cells have limitations in their structure and geometry using traditional manufacturing methods. 3D printing can significantly reduce the production costs by preventing loss of expensive materials and simplifying the number of equipment used in solid oxide fuel cell manufacture [38,39]. In a study using 3D printed ceramic corrugated membranes, the performance of fuel cell and electrolysis modes was increased by 57%. Furthermore, 3D printing as a manufacturing method is promising as the 3D printing precursor in the same machine can be altered to produce carbon [28] or ceramic materials [39].

To create carbon microstructures from polymer materials, many research studies use a pyrolysis procedure under an inert atmosphere [28,40,41]. During polymer heating above its degradation temperature, bonds in the carbon chain break and volatile components such as methane are released. In an inert atmosphere such as nitrogen, the carbon is left in an network of graphene fragments [42]. At higher temperatures (>800 °C), the defects in these networks are removed, which increases crystal and stack size, in turn increasing electrical conductivity. If oxygen is present, material combustion could occur and CO_2 or CO will be produced in a charring process. Small volatile molecules are released as bubbles, which could create deformation in the carbon structure. Studies which aim to preserve the microstructural features heat the 3D printed samples slowly in nitrogen to around 900 °C [28,40,41].

Materials obtained from biological sources have also been carbonised using a similar pyrolysis processes [43]. This has been shown to produce activated carbon type materials from lignocellulosic materials (e.g. bamboo) which have a high specific surface area suitable for supercapacitor electrodes [43—46]. However, the pore scale characteristics (e.g. pore throat size) cannot be controlled compared to 3D printed methods. Although, Bio-based materials such as bamboo has a unique structured porous system that exibits anisotropy in effective properties [46,47]. The magnitude of electrical conductivity produced by these materials increases with pyrolysis temperature but is relatively low (5 S m^{-1}) [47] compared to commercial carbon paper. The shrinkage during

pyrolysis in polymer materials (due to material loss) can also be maintained under controlled operation, where pore scale dimensions decrease with increasing pyrolysis temperature [48].

In hydrogen storage applications, increasing the carbonisation temperature with chemically activated carbon fibres can decrease the surface area and porosity [49]. For carbon paper GDL, electrical conductivity can be improved through additional carbonisation steps using temperatures of up to 1350 °C [10].

However, with several of these biological or synthetic materials, the control of the exact distribution of pore sizes and positions cannot be guaranteed. 3D printing methods offer control of device and porous structure geometry for potential optimisation of manufacturing or efficiency [28,39]. To be implemented in PEMFC, the issue of scalability and accuracy of the 3D printing material needs to be addressed. To date, the largest 3D printed electrode used in a microbial fuel cell is of 6.25 cm diameter and 1.15 cm thickness [28]. This thickness is too large for PEMFC applications and should be reduced to enable implementation of 3D printed materials.

This study uses 3D printing to design and carbonise a porous microstructure that has features necessary for it to perform as a GDL. This material is then integrated into a laboratory scale membrane electrode assembly and tested in a low temperature fuel cell as shown in Fig. 1 (d). This study serves as a foundation for 3D printed carbon gas diffusion layer research. The structural features of the manufactured material are analysed, demonstrating:

1. The importance of pyrolysis process setting to achieve an accurate carbon structure
2. The dimensions achievable in the material (pore, fibre and material size)
3. The electrochemical performance deterioration caused by ineffective membrane coupling and damage

Methodology

The design and manufacture process for the 3D printed based GDL is highlighted in Fig. 2. Firstly, a custom code was developed to generate anisotropic large scale lattice structures and extract the surface (.stl file shown in Fig. 2 (a)) required for the 3D printer (Fig. 2 (b)). The 3D printed structure had a limitation of 5 cm side length due to the diameter of the tube in the muffle furnace as shown in Fig. 2 (d). The material was carbonised using a pre-determined set of temperature increments in order to maintain structure accuracy, with a glassy carbon structure being produced as shown in Fig. 2 (e). 5 wt% PTFE was added to the structure in order to coat the surfaces and increase the hydrophobicity (shown visually as the white parts in Fig. 2 (f)). A suspension of MPL and CL was sprayed and dried onto one side of the structure as shown by the microscope image in Fig. 2 (g). The cell was finally assembled through hot-pressing to form the MEA with the material set up shown in Fig. 1 (d).

Materials

Polytetrafluoroethylene (PTFE) dispersion (60 wt%) was purchased from Sigma–Aldrich. Ketjen black was purchased from EC–300J, AkzoNobel. Toray carbon paper (TGPH 090) was purchased from The Fuel Cell Store. PTFE film (0.2 mm thickness) was purchased from Goodfellow. 60 wt% platinum supported on high surface area carbon catalyst (Pt/C, Alfa Aesar).

3D printing

The 3D printing resin used in the ELEGOO MARS UV LCD printer was the clear green water washable uv-curing resin 405 nm (Elegoo). The reservoir shown in Fig. 2 (b) is filled with the UV curable resin. This contains a clear fluorinated ethylene propylene (FEP) film on the bottom surface which separates the LCD screen with 50 μm pixel resolution from the resin. The ordered lattice structure is oriented appropriately onto the plate (with a support raft attached to the plate) and sliced with a layer height of 20 μm. The 3D printer was operated with an exposure time of 8 s, with 5 bottom layers at an exposure time 60 s. The lift and retract speed of the plate was 100 and 150 mm min^{-1}, respectively. The print time for one piece of material of 5 × 5 cm^2 in size was approximately 1 h.

During the development stage, different 3D printed structures (with varying fibre and pore diameters) were generated as shown in Fig. 3. From the images, it is clear there is a limitation on the practical size of the lattice features. Fig. 3 (a) shows that some of the fibres achievable consisted of 2 pixels (100 μm which in most cases would break off from the structure). This structural damage is visible in Fig. 3 (f), and shows that there is a minimum reachable feature size of approximately 5 × the printer resolution (i.e. 250 μm fibres to ensure mechanical stability). This is especially important during printing, where stress is introduced via detachment from the FEP film and during handling and carbonisation steps. Nevertheless, using a cheap desktop 3D printer, micron sized features were able to be incorporated into the structure. The rough fibre surface area shown in Fig. 3 could provide benefits for redox flow batteries where the increased surface area would increase the reaction rate [30].

Carbonisation

The 3D printed material shown in Fig. 2 (c) was carbonised in nitrogen flow using a Carbolite muffle tube furnace (Fig. 2 (d)). The first tests used settings from other similar procedures reported in literature [50] (starting at room temperature and increasing to 900 °C at 10 °C min^{-1}), but as shown by the results in Fig. 4 (c), this caused significant deformation and swelling which consequently cannot be used in PEMFC as a GDL. Using a temperature ramp rate that is high will cause increased gas release during phase change from solid polymer to voltile species. These are produced inside the polymer fibres and expand to deform the structure [42,50]. Different resins will have varying amount of volatile release and therefore it is important to perform thermal analysis to control the decomposition process.
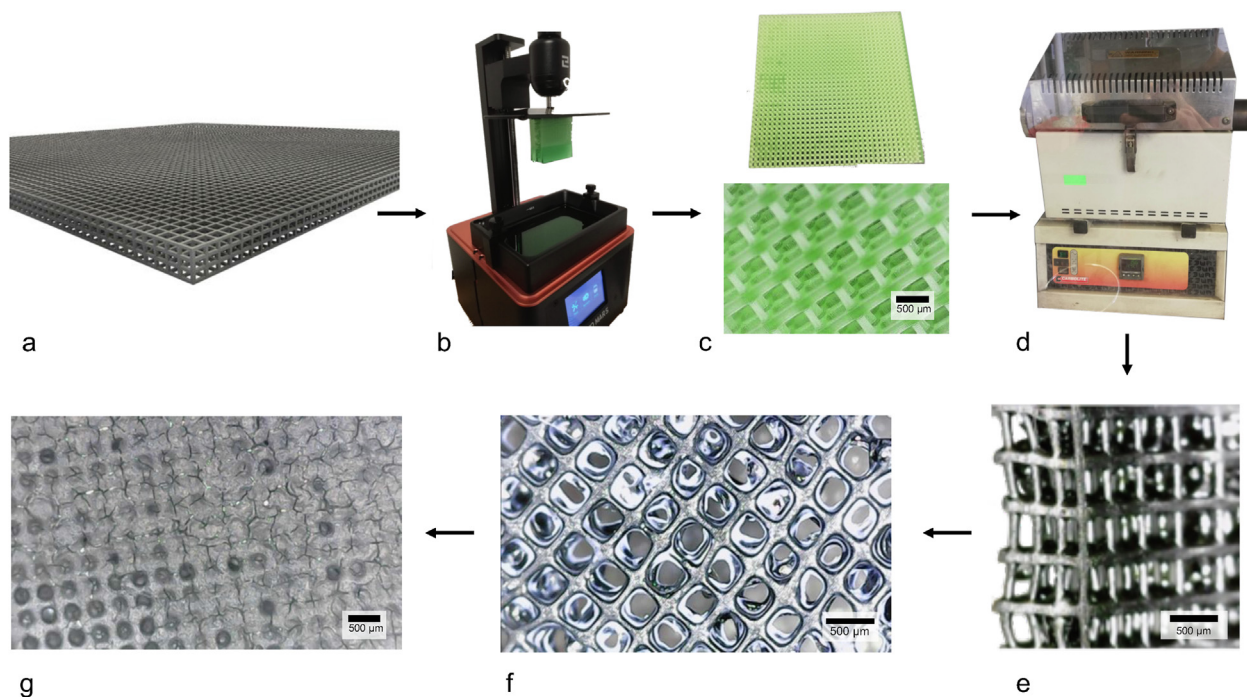
Fig. 2 – Process workflow to manufacture 3D printing GDL. (a) rendering of digital design using custom code, (b) desktop UV 3D printing of digital structure, (c) images of printed macro and microstructure, (d) Carbolite muffle tube furnace used for carbonisation step, (e) image of carbonised 3D printed structure, (f) Wettability alteration using PTFE, (g) MPL and CL application to the surface.
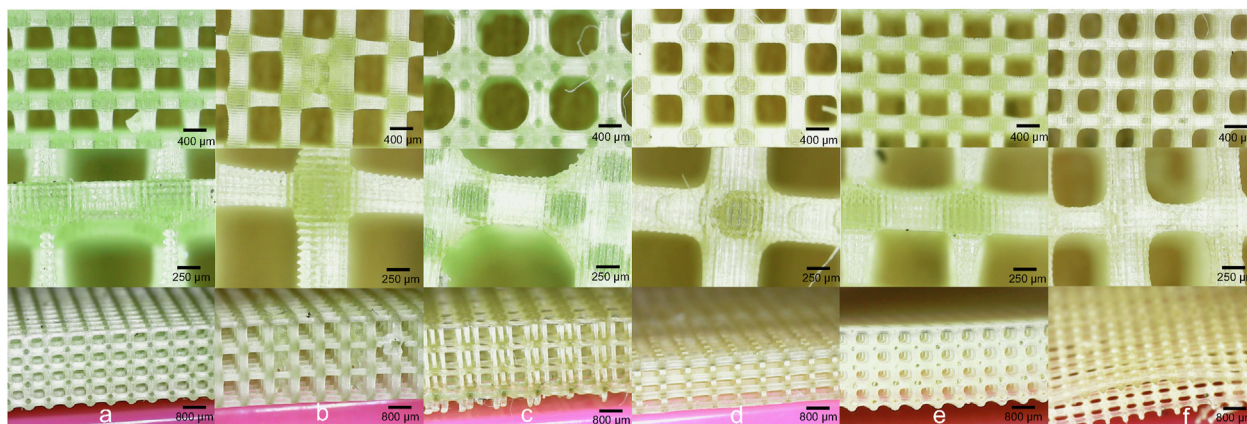

Fig. 3 – Optical microscope images for different 3D printed rectangular lattice structures (a–e). Columns of images show the same microstructure at different magnifications and the last image shows the side view of each material.

A sample of the cured UV resin was analysed in a thermogravimetric analyser (Discovery TGA 550) producing the mass loss profile as shown in Fig. 4 (a). The TGA was conducted using a temperature ramp rate of $10\,^\circ C\,min^{-1}$ to $900\,^\circ C$ as this covers the range of temperatures achievable in the tube furnance. The results show that there were three phases of material mass loss and therefore structural change: 1) ($25–300\,^\circ C$) likely contributes to water vapour production with a 10% mass loss, 2) ($300–500\,^\circ C$) significant mass loss associated with pyrolysis of volatile components with 80% mass loss

and 3) ($500–900\,^\circ C$) no mass loss but with energy being used to reorder carbon crystal arrangements to a more favorable electrically conductive state (i.e. glassy carbon) [42,50]. Using the information provided by the TGA, the process settings for the furnace was chosen as shown by 4 (b). In order to reduce structural damage, temperature ramp rates were decreased or held during temperature ranges of increased mass loss. In total the carbonisation time was 11 h; however this time could be improved by using a faster temperature ramp rate during stages 1 and 3 (below $300\,^\circ C$ and above $500\,^\circ C$), but this was not
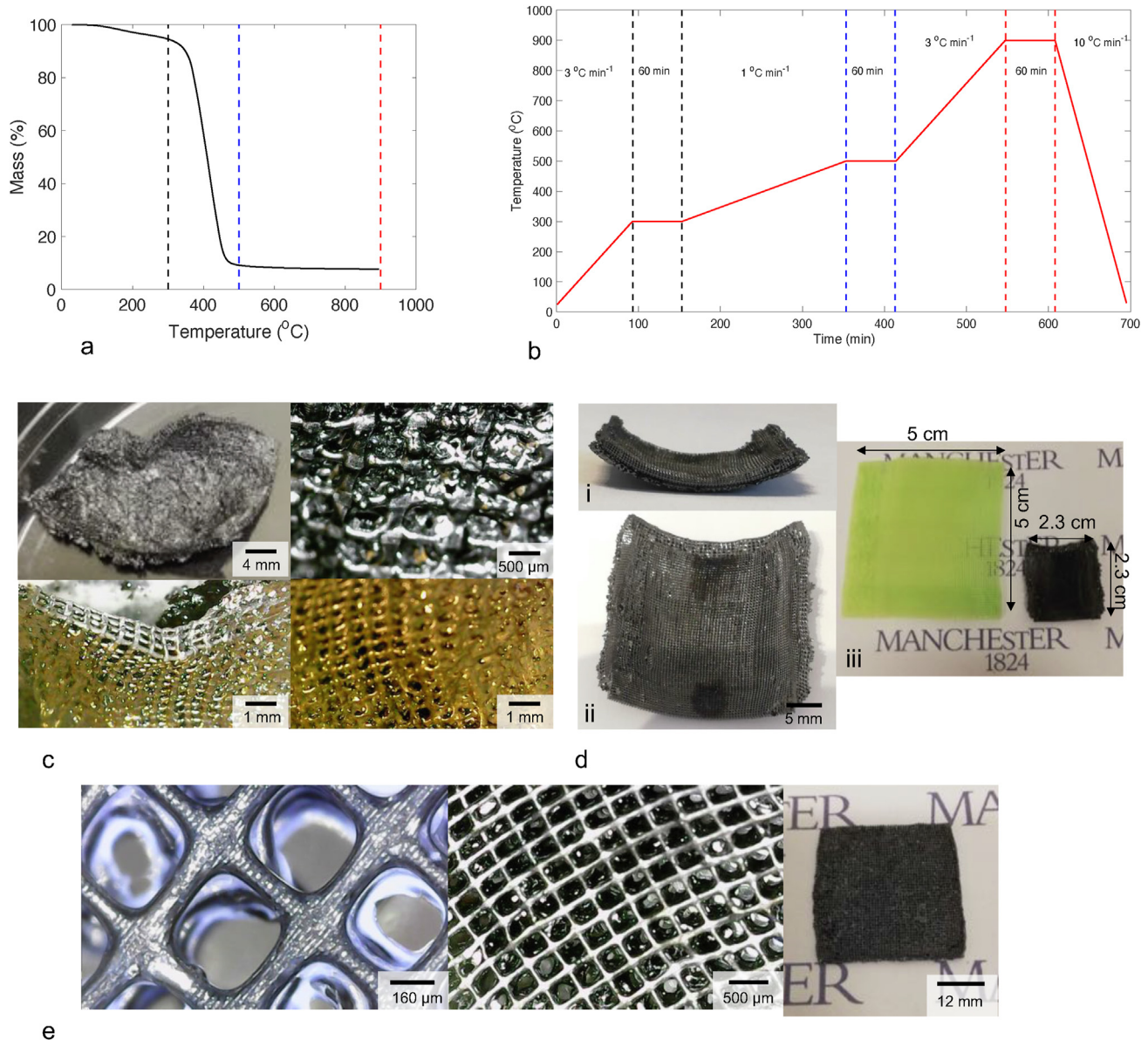
Fig. 4 – (a) mass loss (%) with temperature extracted from thermogravimetric analysis of the polymerised 3D printed resin. Dashed lines represent the temperature set points of 300 °C (black), 500 °C (blue), 900 °C (red). **(b)** processes operating temperature of the tube furnace for the carbonisation process, with ramp rates or dwell times highlighted. **(c)** first carbonisation of a 3D printed structure without controlled furnace settings. **(d)** successful carbonisation with deformation, showing isotropic material shrinkage. **(e)** microscope images of final structure taken further in the study. (For interpretation of the references to color in this figure legend, the reader is referred to the Web version of this article.)

tested in the current study. The samples were placed on 4.8 × 5 cm plates in order to ensure the material retained a flat form during the carbonisation step; if left in the tube without a flat support, the structure can warp to the curvature of the tube as shown in Fig. 4 (d) (i) and (ii).

After carbonisation, the 3D printed material shrinks to approximately 46% of the original size. After inspection of different carbonised structures, the shrinkage appears to be isotropic as shown in Fig. 4 (d). Using the settings in Fig. 4 (b), structure accuracy at micro and macro-scales is seen to be maintained in Fig. 4 (e).

The material was coated with PTFE 5 wt% to improve its hydrophobicity. This is also similar to the 5 wt% coating found in the commercial Toray material. This was performed by making up a solution of PTFE 10 wt% from a 60 wt% solution by addition of de-ionised water and subsequent dipping of the material in the solution under sonication for 1 min. The material was then dried in an oven at 70 °C. This process was repeated until the new total mass was 5% higher than the original weight. The electrical conductivity was measured using a two-point probe method [51] using a RS PRO IDM67 Handheld Digital Multimeter.

3D electrode preparation

To assemble the membrane electrode assembly (MEA) 1.5 cm × 1.5 cm of carbon paper was cut as the gas diffusion layer (GDL). Ketjen black, mixed with 60 wt% PTFE (the weight ratio of Ketjen black and PTFE is 90:10) in 17 ml IPA, was deposited on the GDL by nitrogen-spraying to form the 1 mg cm^{-2} microporous layer (MPL) followed by sintering at 300 °C for 3 h. Then, catalyst layer (CL) ink, composed of 85% of Pt/C and 15% of 20 wt% Nafion in 10 ml acetone as solvent, was deposited on the MPL by nitrogen-spraying to form 0.25 mgPt cm^{-2} loading on both the anode and the cathode. To evaporate organic solvents (IPA and acetone), the electrodes were dried at 120 °C during spraying for both MPL and CL. Afterwards, 0.5 mg cm^{-2} Nafion bonding layer was sprayed on the catalyst layer. Finally, two electrodes (same catalysts on both anode and cathode sides) with Nafion-212 were used to prepare the MEA by hot-pressing at 135 °C for 2 min and at 80 psi for another 2.5 min pressing at the same temperature [52]. For the MEA performance tests, the single fuel cell (1.5 cm × 1.5 cm electrode area) was put between two graphite plates of size 40 mm × 40 mm × 20 mm the serpentine gas channel in the centre of the graphite plates is of size 13 mm × 1 mm × 1 mm (Figure S1) [53]. For the reference commercial MEA, carbon paper was used as the GDL in the cathode and anode whereas in the 3D printed based MEA, the 3D printed material was used as the cathode GDL (shown in Fig. 1 (d) and implemented into the MEA using the same method.

The fuel cell was tested under 100% relative humidity for 100 ml min^{-1} of both H$_2$ and O$_2$ without back pressure. During the cell activation step, the fuel cell was activated by scanning the current from zero to the maximum current for 5 times at room temperature, 30 °C, 40 °C, 50 °C and 60 °C. The results were recorded by scanning the current from zero with the higher open circuit voltage (OCV) to the maximum current point. The current scanning step is 0.01 A s^{-1}, staying at each point for 30 s.

Electrochemical impedance spectroscopy (EIS) measurements were conducted using a Gamry Interface 5000 E at different temperatures under 100% relative humidity for 100 mL min^{-1} of both hydrogen and oxygen without back pressure. The impedance spectra were recorded at a constant voltage of 0.40 V by sweeping frequency between 10 kHz and 0.1 Hz with AC signal amplitude of 100 mV and recording 10 points per decade. Gamry Echem Analyst software was used to fit the EIS curves to obtain the equivalent circuits. The linear sweep voltammetry (LSV) was also tested by Gamry Interface 5000 E when the hydrogen and nitrogen were fed to anode and cathode at the flow rate of 100 mL min^{-1}, respectively. The cathode works as the working electrode at 2 mV s^{-1} from 0 to 0.8 V against anode [2].

For post-electrochemical testing analysis, the 3D based MEA was freeze−fractured in liquid nitrogen and cut by a disposable scalpel No. 20 (Swann Morton). The surface and cross−section of the GDL was studied by scanning electron microscopy (SEM, Quanta 250 equipped with an Energy Dispersive X−ray Spectroscopy (EDS) detector (Oxford Instruments).

Simulations

To investigate further the combined effect of a 3D printed GDL lab scale flow field on the oxygen distribution, two computational fluid dynamics simulations were set up. The serpentine flow field is shown in Fig. 5 (a) which was used to generate the computational mesh shown in Fig. 5 (b). The air is introduced to the inlet plane (green) and leaves through the outlet channel (red). The porous domain and channels are fully connected in both simulations, which used different pore scale structures as shown in Fig. 5 (c). The ordered porous structure and carbon paper reconstructed sample were created using a voxelised porous microstructure generator code in MATLAB [8]. The ordered structure (1 mm) was 2.6 times thicker than the carbon paper material (380 μm) investigated. The lattice spacing between pores was 350 μm.

The computational mesh used a surface refinement mesh, with a resolution of 23 μm for the porous structure and 47 μm for the channel, with a total of 2 million cells for the 3D printed and 5 million cells for the carbon paper simulation. Assumptions of incompressible, steady-state, isothermal conditions for the air phase were used to solve the Navier-Stokes equations using the simpleFoam solver (OpenFOAM) to find the velocity and pressure field with model details found in Ref. [9]. As a post processing step, a passive scalar was transported from the inlet to the outlet using the convection diffusion equation with a fixed flux boundary at the CL surface.

The diffusion coefficient D of oxygen in air was set to 2 × 10^{-5} m^2 s^{-1} and the gradient of oxygen at the CL surface was

$$\nabla C = -\frac{i}{4FD}, \tag{1}$$

where F (96 485 A mol^{-1}) is the Faraday constant and i is the current density (10 000 A m^{-2}). This boundary condition was set to approximate the oxygen consumption process at an operating current density of 1 A cm^{-2}. Water production was ignored because the computation time of such simulation would be very expensive in regards to the purpose of the simulation [9].

Results

3D printing and carbonisation

The process of converting a digital design of an ordered lattice microstructure to a 3D printed result is shown in Figs. 2 and 3. Only one microstructure was taken forward to integrate into the lab scale fuel cell due to time constraints. Other materials that were carbonised had suffered deformation of the structure, and would not make a good candidate to test in the fuel cell.

The properties of the 3D printed lattice structures before and after carbonisation are shown in Table 1. The permeability of the 3D printed structure was predicted using the analytical equation in Ref. [54] and was 213 times higher than the permeability of carbon paper materials [8]. The effective diffusivity was found using CFD simulation on different
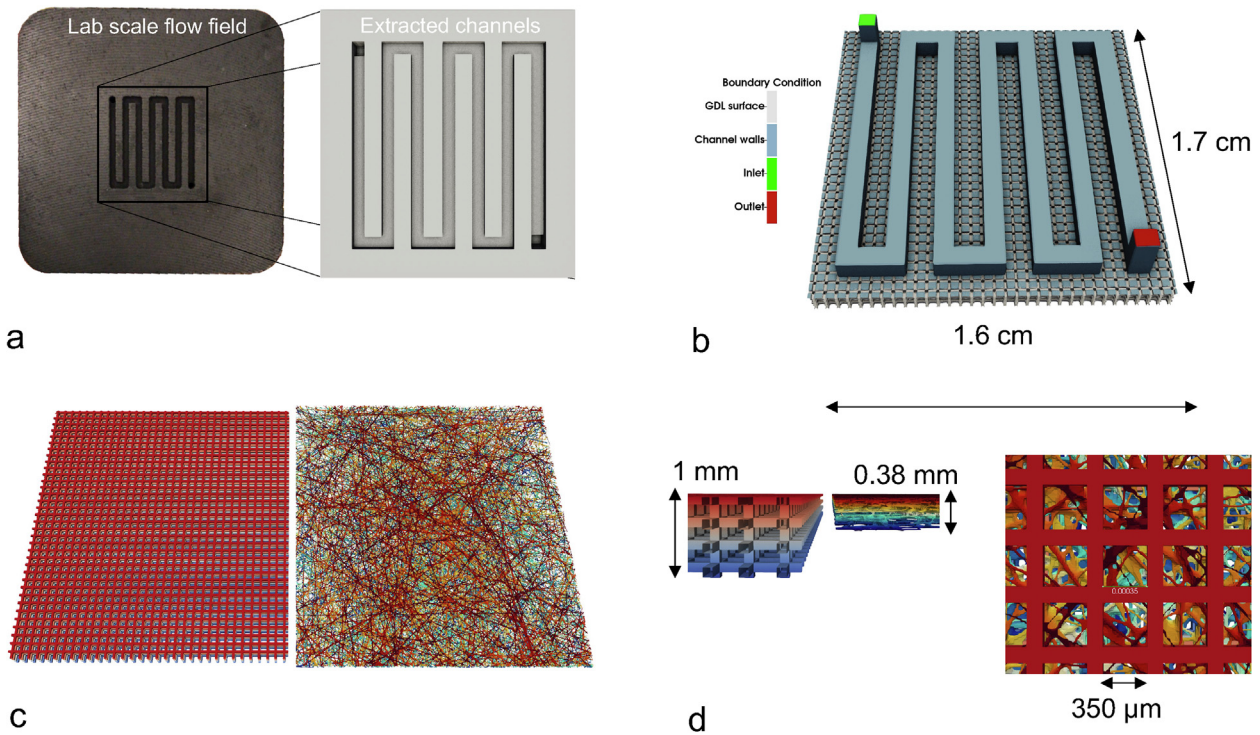
Fig. 5 – (a) Image of the lab scale fuel cell with the channels extracted for the simulation domain. (b) simulation domain showing the inlet (green), outlet (red), channel walls (blue) and porous GDL surfaces (grey). (c) Porous structures used in the simulations represent the 3D printed and carbon paper materials. (d) Close up of porous microstructures, showing thickness and pore size differences. (For interpretation of the references to color in this figure legend, the reader is referred to the Web version of this article.)

The measured electrical conductivity was low at 150 S m^{-1}. However, this measurement is likely contaminated by the inability of the two probe method to account for contact resistance. We anticipate the actual conductivity to be on the order of 1000 S m^{-1} [57], since the carbon produced has a similar conductivity to highly orientated pyrolytic graphite [58].

SEM analysis of carbonised GDL

SEM and optical microscope images of different carbonised 3D printed GDL are shown in Fig. 6. The figure shows different materials in the rows and the columns show different magnification. The last image in Fig. 6 (a - b) shows the catalyst coated side of the microstructure. The results show that the carbonised material maintains its structural accuracy over a large scale and that the material surface is reflective like graphitic carbon. Resulting from the straight though pore design, application of the MPL and CL onto one side of the structure (shown in Fig. 6 (a)) thickens the fibres and does not form a smooth layer, with MPL cracks resulting from spray drying process. The material shown in Fig. 6 (b) shows a structure with smaller pore sizes. During the coating stage, PTFE accumulated at the bottom surface of some pores (shown by the white regions) which impacts significantly the oxygen transport to the catalyst layer. Although with this design the catalyst layer formed was smoother and had less holes, which indicates that a smaller pore size could form a flat CL surface.

Table 1 – Summary of material characterisation results for the 3D printed material before and after carbonisation processes.

Material	3D Printed	3D Printed Carbonised
Electrical conductivity (S m^{-1})	0	150
Permeability (m^{-2})	1.92×10^{-8}	4.80×10^{-9}
Effective Diffusivity	0.81	0.81
Contact Angle (°)	55 ($\pm$10)	89 (110 with 5 wt% PTFE) ($\pm$10)
Minimum pore size (μm)	400	200
Thickness (μm)	1000	411
Porosity	0.88	0.88 (0.65 after CL)

lattice structures by increasing the fibre diameter using a similar method to Ref. [8] and is found to be 38% larger than the maximum diffusivity of a commercial GDL sample [55]. The contact angle was measured using the sessile drop method [56] with a 33 μL droplet placed on the surface and using image analysis to estimate the contact angle which ranged from 55° for the raw 3D printed material, 89° after carbonisation and 110° after PTFE coating. Due to the roughness of the surface microstructure, the contact angle had a variability of $\pm$10°.
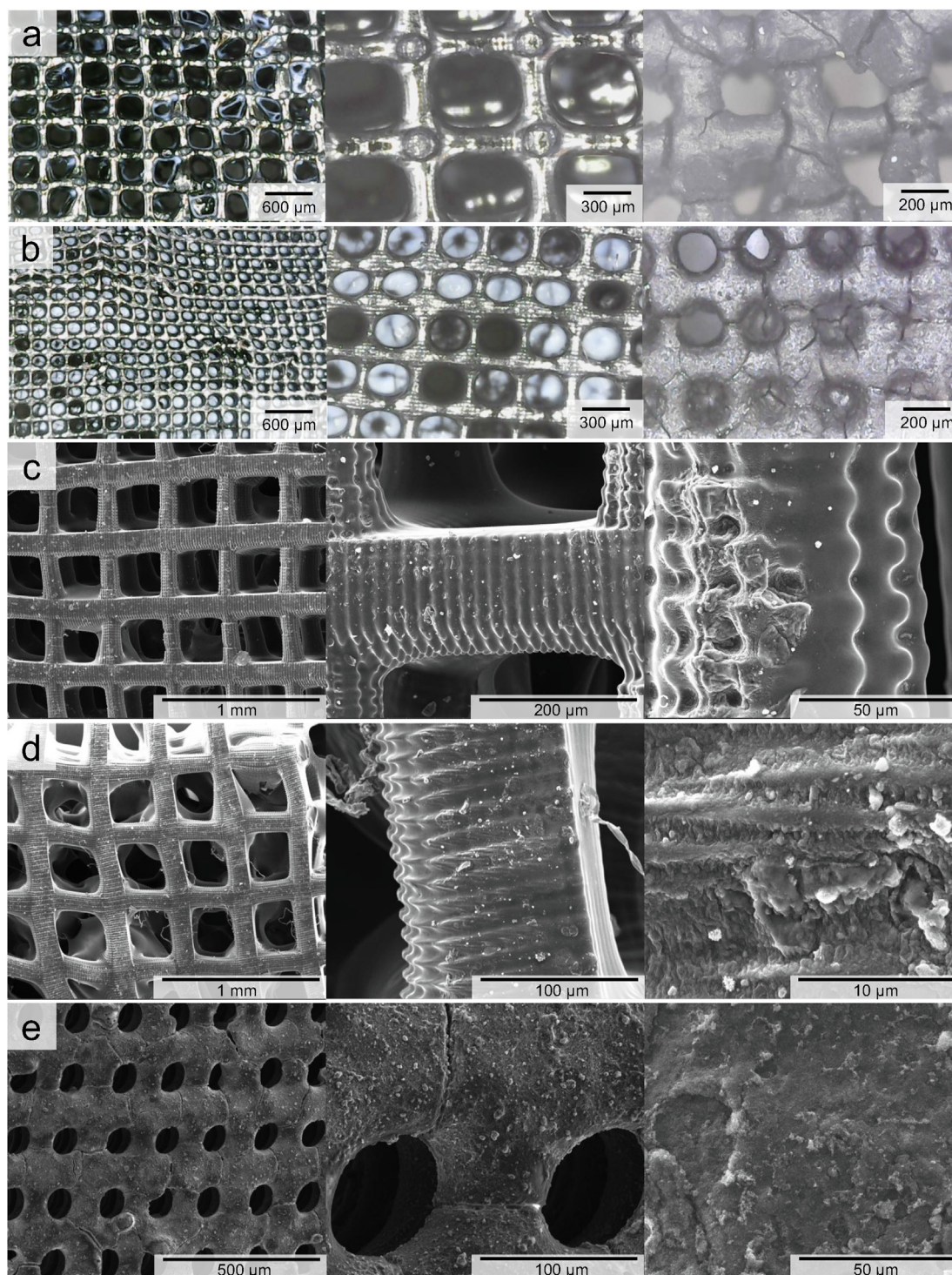
Fig. 6 — Optical microscope images of different carbonised structured GDL samples with columns showing different magnifications. (a) contains a larger pore size than (b) which has more PTFEand sample 2 (e—f) where the coated PTFE can be seen in white.

SEM images of other carbonised 3D printed structures are shown in Fig. 6 (c - e). These images provide higher resolution images to demonstrate the structural accuracy maintained during the carbonisation procedure outlined in Fig. 4. Interestingly, the fibres of the lattice are not smooth; there is an induced surface roughness caused as an artefact of the 3D printing. This microstructure effect can be seen in the 3D printed structures prior to carbonisation such as in Fig. 3 (b). This higher surface roughness may be beneficial for the use of 3D printed carbonised structures in redox flow batteries (where the reaction rate increases with surface area) [30] or for microbial fuel cells [28]. Fig. 6 (j - l) show an image of the

catalyst coated side, illustrating how the MPL coats and thickens the fibres. As future work, it is possible to show that there is a limit to the pore size that will allow an efficient integration of the material into PEMFCs.

Polarisation curve

A membrane electrode assembly was created from the 3D printed electrode (cathode), carbon paper (anode) and Nafion 212 (membrane). This was tested in a low-temperature hydrogen fuel cell as shown in Fig. 1 (d). References to the 3D printed carbonised GDL will be referred to as "3D″, whereas reference to the commercial carbon paper (Toray) will be referred to as "Commercial". The performance obtained for all MEAs tested in the fuel cell using the 3D cathode and commercial electrode was shown to increase with higher operating temperature as shown in Fig. 7 (a).

As shown by Fig. 7 (b), the maximum power density obtained for the 3D material (205 mW cm^{-2}) was lower than in the commercial electrode (543 mW cm^{-2}). This can be explained by the low open circuit voltage in the 3D cathode based MEA (around 0.6 V) which is a consequence of severe hydrogen crossover and leads to further deteriorated performance for the 3D based MEA. In the commercial material, there is a sharp decline in the polarisation curve, which is related to high mass transfer loss, especially at higher temperatures [59].

Linear sweep voltemmetry (LSV)

The low OCV exhibited by the 3D MEA can be explained by the hydrogen crossover. Hydrogen crossover occurs via diffusive transport, where the hydrogen concentration on the anode side is higher than that on the cathode side. This can cause direct loss of fuel cell efficiency and can lead to cathode potential reduction and produce harmful radicals. Therefore, hydrogen permeability is an important factor to determine the fuel cell performance. Fig. 7 (c) showed the commercial material has a limiting hydrogen crossover current density which is less than zero, illustrating the Nafion 212 in the commercial MEA performs good as the proton exchange membrane without hydrogen crossover. However, the LSV curve for 3D based MEA (black line) has dramatically increased hydrogen crossover current density. The uneven surface of 3D printed electrode can cause the membrane to swell into the large pores which can lead to breakage or introduction of pinholes. This mechanism has been shown to occur even in commercial carbon paper materials [35] and subsequently resulted in increased hydrogen crossover and decreased OCV. Evidence of this membrane damage can be seen in Fig. 9. This damage could be mitigated by either using a higher resolution 3D printer to produce smaller pore scale features which do not induce as much membrane deformation or by printing a flat microporous layer.

Electrochemical impedance spectroscopy (EIS)

To better understand the electrochemical properties of membranes, the EIS was performed. The EIS spectra were fitted using the equivalent circuit shown in the supporting information (Figure S2). Usually, the EIS curves contain three loops: high frequency loop (anode charge transfer resistance), intermediate frequency loop (cathode charge transfer resistance) and low frequency loop (mass transfer resistance). However, it seems only two arcs exist in these EIS curves as shown in Fig. 7 (d), which is not consistent with the apparent mass transfer loss in the membranes tested at 60 °C (Fig. 7 (a)). This is probably due to the instabilities such as acid content and reactant diffusion in the fuel cell [60]. The resistance between the intercept on the real Z-axis at high and low frequencies is interpreted as the sum of charge transfer resistance and mass transfer resistance of the anode and cathode [61]. The various resistances reflected by intercepts on the real Z-axis in the Nyquist curves are summarized in Table S1. As shown in Fig. 7 (d), both commercial and 3D based MEA showed similar membrane resistances (around 0.16 Ω cm^2). However, the sum of charge transfer resistance and mass transfer resistance for 3D based MEA (0.30 Ω cm^2) at 60 °C had larger resistances than the commercial based MEA (0.19 Ω cm^2). However, since the mass transfer resistance is unlikely to be high due to the large pore sizes, the increased resistance of 3D based MEA may be related to higher charge transfer resistance and contact resistance due to the large pore size and uneven membrane after hot-pressed as shown by the SEM results in Fig. 9. Additionally, the uneven catalyst distributions and low catalyst utilization in cathode may be another explanation for increased charge transfer resistance as will be explained in the analysis of Fig. 8.

Analysis of benefits of 3D printed electrode

Although the 3D printed MEA exhibits low power density, higher hydrogen crossover, and larger impedance than the commercial based MEA, there are still some interesting points based on the electrochemical performance, including the low mass transfer resistance and better water management. To reduce the interference from the different reaction rates and better understand the factors which may cause the polarisation variations, the regions at the same current density for each MEA were compared. As shown in Fig. 7 (e − g), when taking the five polarisation curves during the activation steps, the polarisation curves for the commercial based MEA showed larger variations (ΔV) especially in the high current density region, compared with 3D based MEA.

At higher current density, the rate of reaction is higher and this produces more water which may block the pores in the gas diffusion layer, microporous layer and catalyst layer. This potential variation was also more apparent at higher operating temperature (Fig. 7 (f)) where the 3D printed MEA was more stable than the commercial MEA. Water produced in the cathode side which cannot be immediately removed out of the cathode chamber can block the oxygen pathways and terminate the reactions in the cell. This was shown by some of the polarisation curves in the commercial based MEA which are suddenly terminated during the activation (Fig. 7 (f - g)). This shut-down situation was significantly improved in the 3D based MEA. The repeatable polarisation curves with minimized transient potential variations for the 3D based MEA highlights the potential water management in the 3D ordered structure at the same current density regardless of the lower
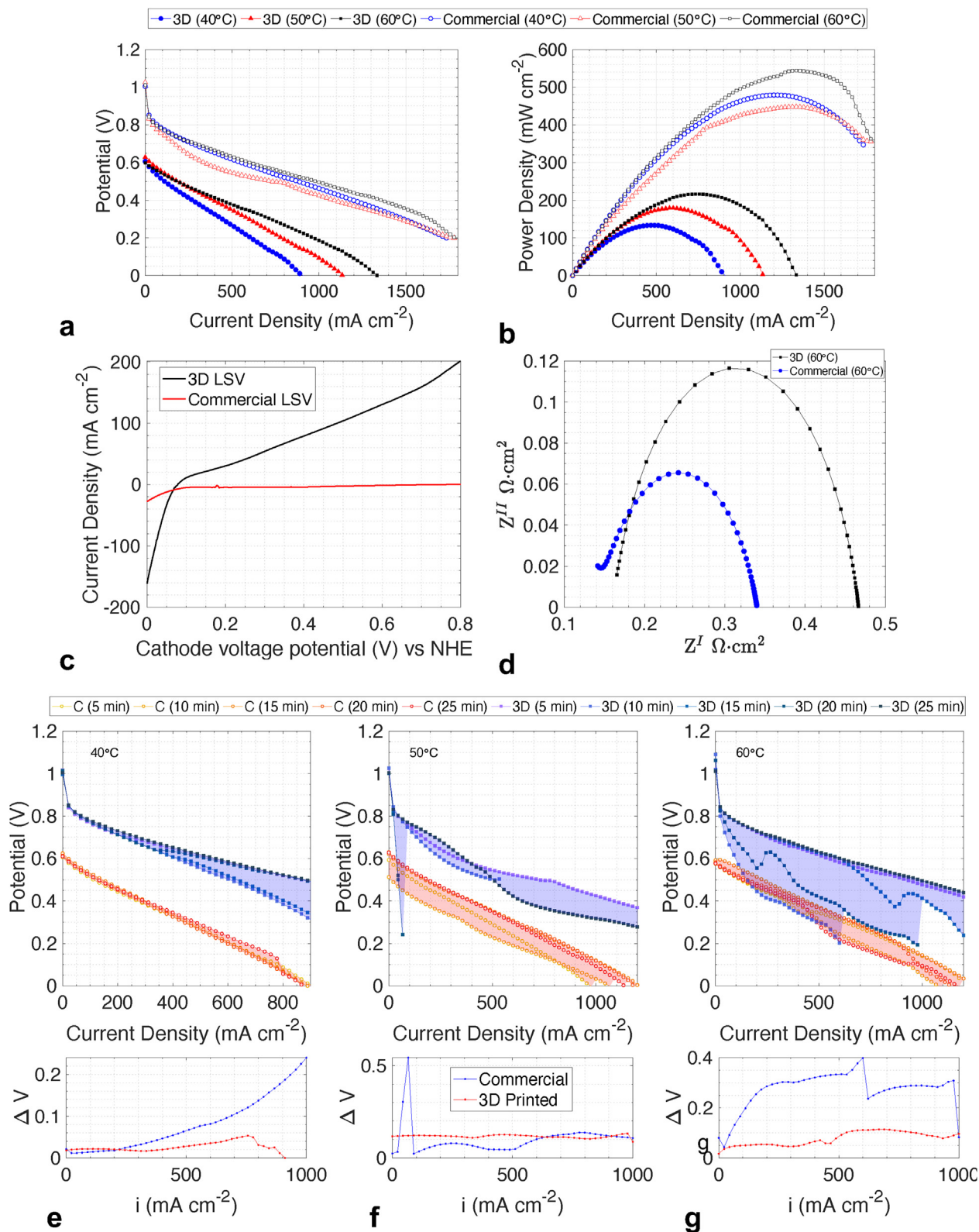
Fig. 7 − (a) polarisation curve and (b) power density for 3D printed and commercial materials between 40 and 60 °C. (c) LSV and (d) nyquist plot for the 3D printed and commercial materials at 60 °C. Variation in polarisation curve measurements (5 min difference) for the 3D printed (3D - red) and commercial materials (C - blue) at (e) 40 °C, (f) 50 °C and (g) 60 °C. Shaded regions show area of variability between measurements, with the magnitude of the variation shown below each column. (For interpretation of the references to color in this figure legend, the reader is referred to the Web version of this article.)

Fig. 8 − (a) SEM of cross section of MEA with the material shown in Fig. 6 (a), with layers segmented by colours. (b−e) SEM and EDS of the 3D printed material cross section without the MEA, (f−i) SEM and EDS of the MEA cross section, showing the elemental distribution of carbon, platinum and fluorine respectively. The SEM and EDS information allowed for the identifications of the distribution of materials in (a). (For interpretation of the references to color in this figure legend, the reader is referred to the Web version of this article.)
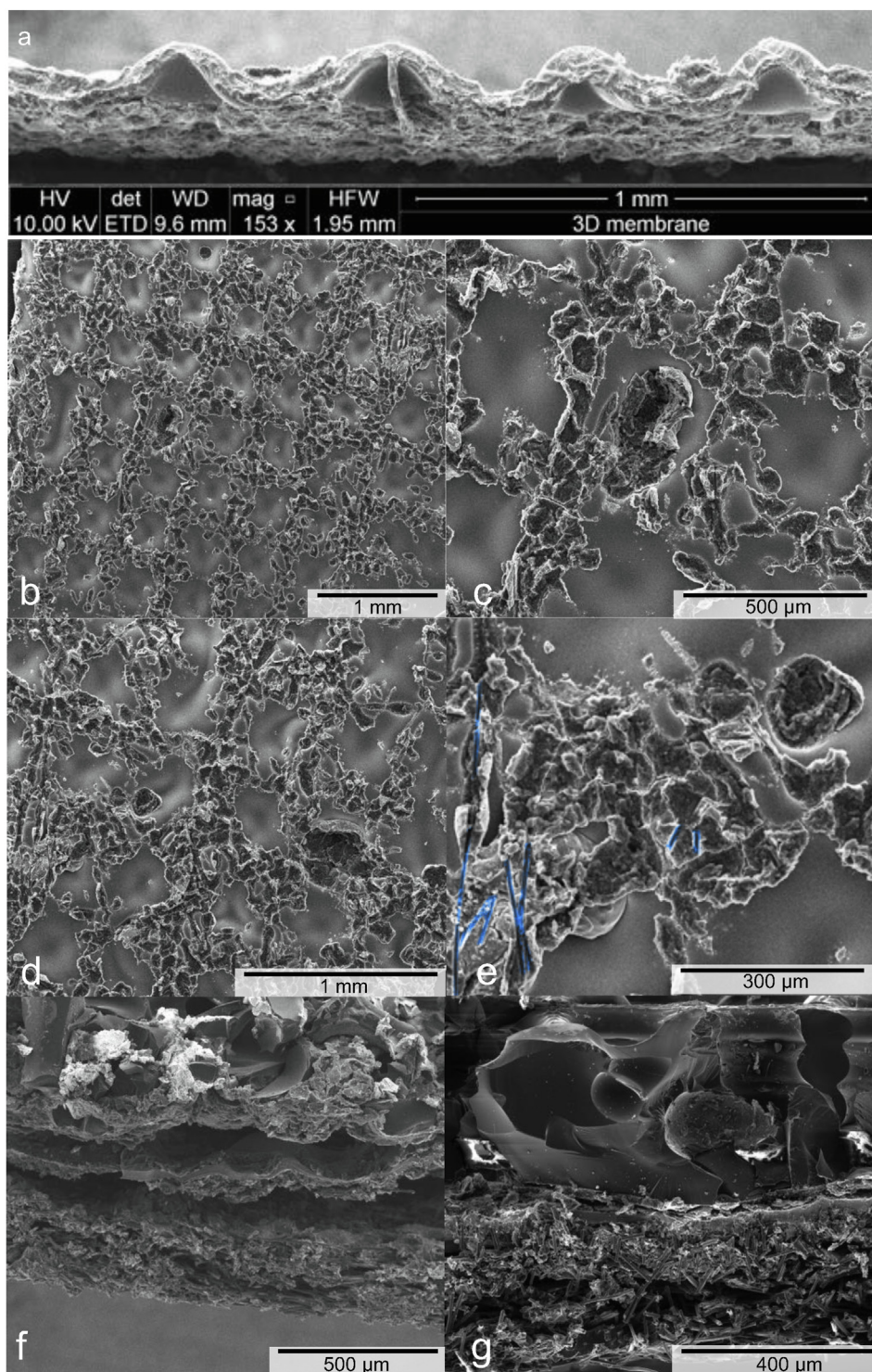
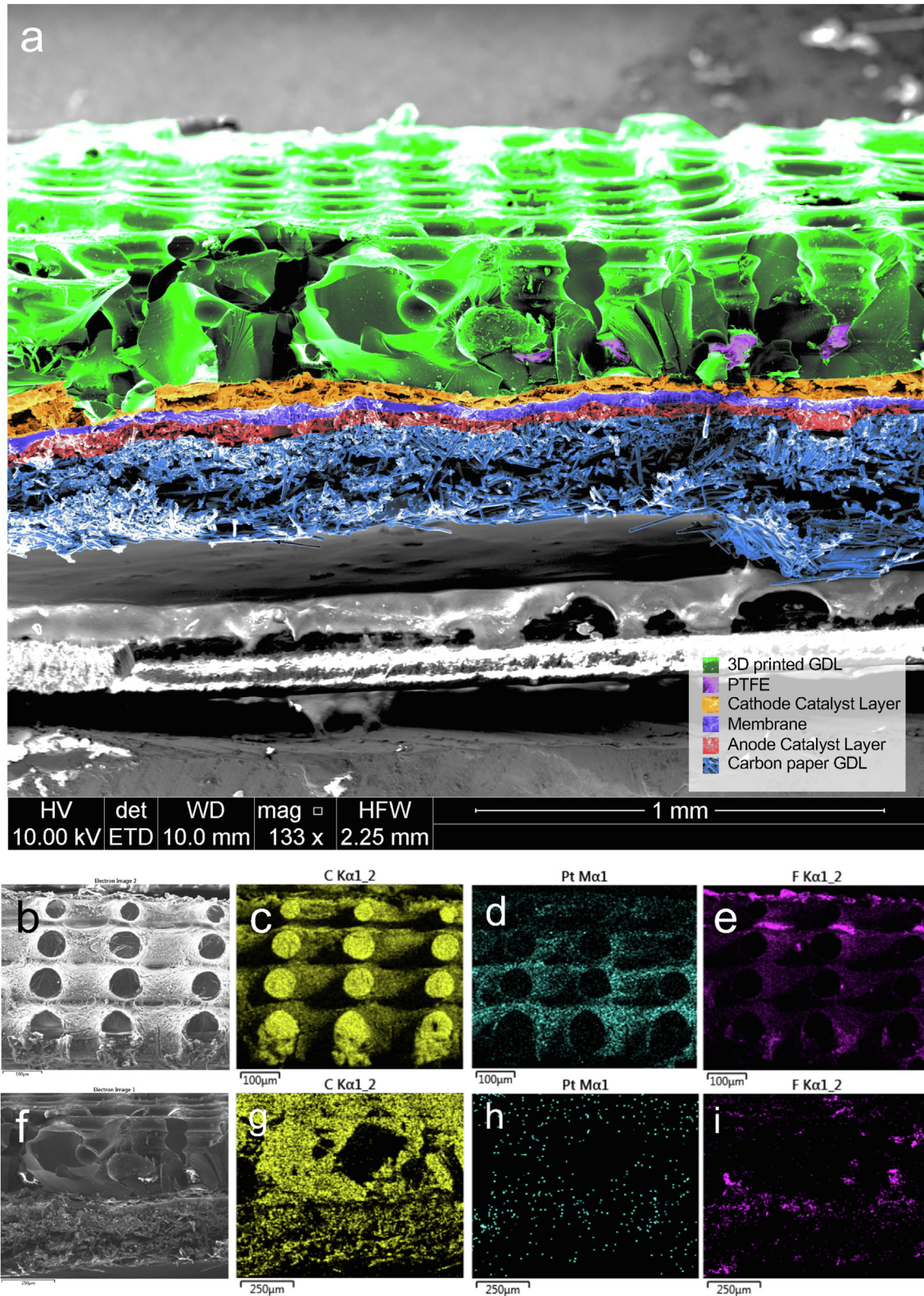Fig. 9 — (a) cross section SEM image of the membrane detached from the 3D printed MEA using liquid nitrogen. The peaks in the curves represent the areas where the large through-plane pores are present. (b) SEM image of the membrane showing the rough contact regions with the 3D printed GDL. (c) magnified region showing potential area of membrane breakage. (d e) highlighted areas (blue) where anode GDL fibres can be seen through the cathode side. (f—g) show the cross section of the MEA where membrane deformation is seen. (For interpretation of the references to color in this figure legend, the reader is referred to the Web version of this article.)

power density (which is a result of the integration with the membrane). All five polarisation curves are successfully measured in the 3D based MEA, compared with only two intact testing in commercial based MEA; where the polarisation curve at some current density in the 3D MEA was higher than the commercial MEA.

Analysis of 3D printed MEA

To inspect the construction of the MEA, SEM and EDS were used to look at the morphology and element distribution. Fig. 8 (a) shows the cross section of the MEA that was cut (which inevitably caused material damage at the edges because of the hardness of the 3D carbonised materials). The different phases of materials can be clearly seen. The 3D printed carbonised material (green) is shown to be successfully integrated with large through-plane pores (140 μm), although the in-plane void space structure appears to be collapsed. Although, as shown by Fig. 8 (b), there is still pore space connectivity in the in-plane direction, its throat size is significantly reduced (35 μm). Furthermore, after cross referencing with the EDS data presented in Fig. 8 (i), there are regions of accumulated PTFE as shown in purple in Fig. 8 (a), which could cause further mass transport losses.

The distribution of PTFE in the 3D printed material can be seen by the analysis of Fig. 8 (e) and (i). The EDS shows that the PTFE is distributed across the surface, but accumulates in certain regions (e.g. at the top surface or inside pore throats). The distribution of PTFE in white is clearly identifiable in the optical microscope images in Fig. 6(a–b) where it either coats the surface more uniformly or can block the pores depending on coating specification. In the commercial material, the distribution of the fluorine containing materials (PTFE) is highlighted to show a greater concentration at towards the membrane and on the external surface, but also distributed inside the material. PTFE in Toray materials will be concentrated at the intersections between fibres and possibly coating uniformly around individual fibres if an optimised coating process is used [24].

The structural changes of the 3D printed electrode from the SEM images shown in Fig. 6 can be attributed to the method of MPL/CL preparation. Fig. 8(b–e) shows the elemental distribution of carbon (c), platinum (d) and fluorine (e) for the cross section of the 3D printed material without the membrane. It is clear from these images that a smooth CL is not created and therefore much of the sprayed MPL is deposited inside the internal structure, which thickens the fibre diameter (shown by increasing fibre diameter with thickness of material from 83 to 44 μm). This is indicated by the distribution of platinum and fluorine (constituents of the CL and PTFE respectively), which are found inside the internal structure. Particularly with platinum distribution in Fig. 8 (d), there is a clear gradient in colour intensity from the CL to the channel side. If an ionomer layer exists in this internal structure, the diffusion path length is large, which will induce significant ohmic resistances; essentially, the effective catalyst active area is under utilised. Furthermore, it is clear from the distribution of fluorine containing PTFE from Fig. 8 (d) the MPL is thickening and blocking the in-plane pore throats of the material.

The images from SEM and EDS shown in Fig. 8 (f - i) were used to identify regions in Fig. 8 (a). These show the distribution of carbon, and fluorine containing PTFE and membrane materials which help identify areas of accumulation and the regions that likely correspond to the membrane.

The collapsing of the void space in the in-plane directions will interfere with effective oxygen transport under the rib regions of the cell, which could increase mass transport overpotential. Taking the information from Fig. 8 it is surprising that the performance of the cell shown in Fig. 7 (a) was achieved, which gives confidence for future research into 3D printed GDL if the challenges encountered in this study are addressed.

Membrane damage

The low OCV exhibited by the 3D printed MEA is the reason for the low power density relative to the commercial based MEA. The state of the membrane in the 3D printed MEA was analysed by removing the membrane from the MEA by doping in liquid nitrogen. SEM of the cross section of the membrane is shown in Fig. 9 (a), which shows the deformation of membrane into the areas where the large pores of the 3D printed structure would be. As shown by research into membrane swelling and deformation, even in commercial GDL this can occur [35] but its effect is amplified in the ordered structures used in our study because of the large through-plane pores. The deformation of the membrane can cause high contact resistance and hydrogen crossover (as cracks and pinholes are likely to occur).

Additionally, as shown by Fig. 9 (b - c) the contact area between the cathode catalyst layer and the membrane (shown by the rough areas) is significantly reduced (only 46% in contact). This firstly underutilises the effective membrane contact area, but also allows areas of uneven compression, leading to eventual breakage and areas of hydrogen crossover. Fig. 9 (d - f) show an area of the membrane where the fibres of the anode carbon paper fibre GDL can be seen through the membrane, which clearly highlights a thin or damaged membrane in those areas, compared to the smooth areas shown in the middle of the pore regions. The membrane deformation and damage which led to the low OCV, high contact resistance and hydrogen crossover can also be highlighted in other cross sections of the 3D printed MEA shown in Fig. 9 (f - g).

To fully understand the potential performance of ordered structures, integration of a smooth CL on the surface must be achieved.

Simulation results

Using computational fluid dynamics (CFD) the idealised performance in terms of oxygen distribution in the cathode flow field and GDL can be investigated.

Fig. 10 shows the results of the steady-state flow and transport simulation performed in the lab scale cell set up shown in Fig. 5. This was performed at a current density of 1 A cm^{-2} and with a 3D printed GDL thickness of 1 mm, which was three times larger than the actual manufactured result. Nevertheless, this analysis shows the improvements to oxygen distribution in the lab scale set up using a 3D printed GDL.
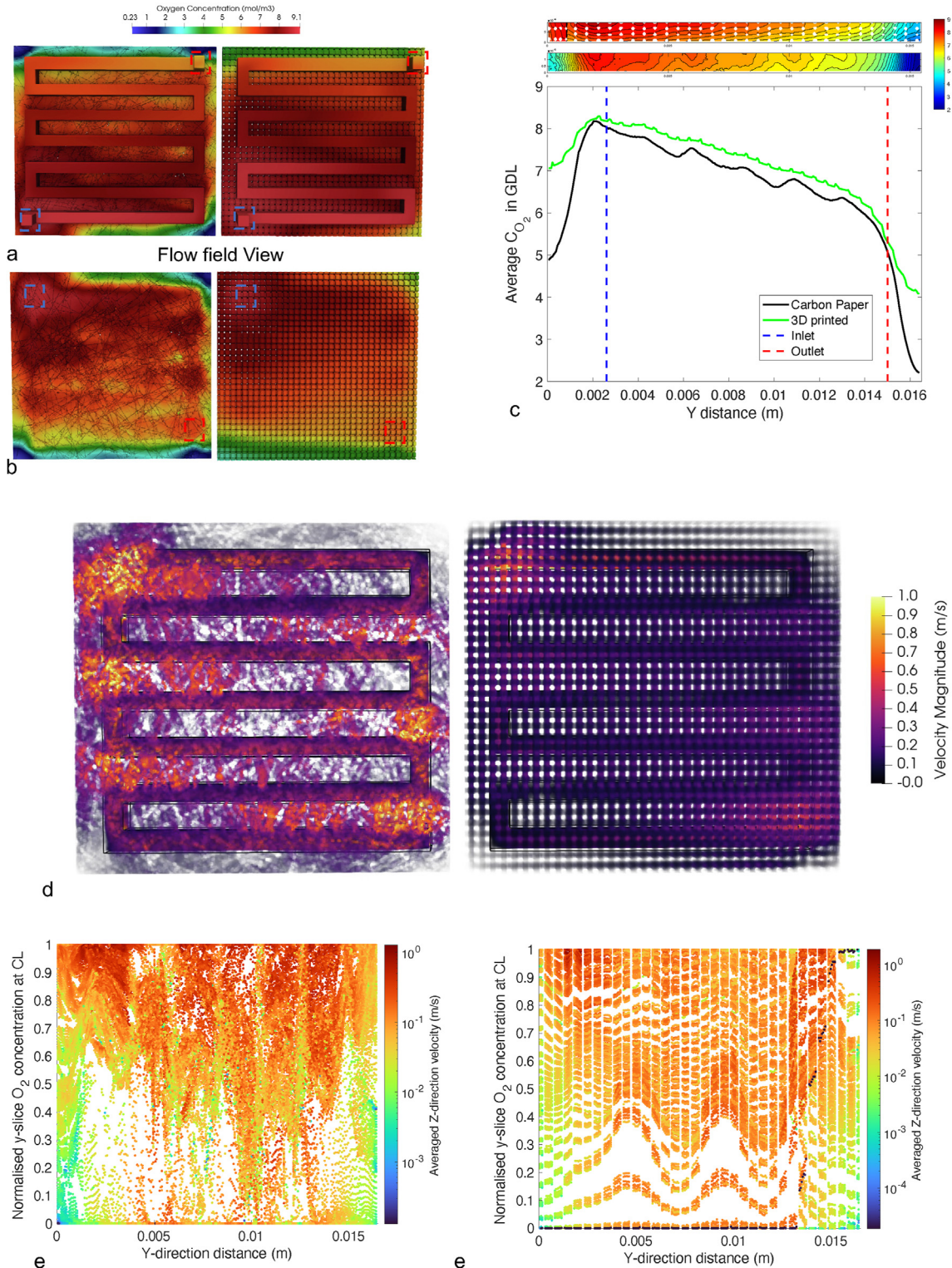
Fig. 10 − (a) flow field view and (b) catalyst layer view of the steady-state flow, oxygen transport and consumption at a current density of i = 1 A cm^{-2}. Inlet and outlet shown in blue and red dashed areas respectively. (c) X-direction averaged concentration in the GDL for the 3D printed (green) and the carbon paper (black) along the Y-direction (from inlet to outlet). (d) velocity magnitude heat map under for both materials (showing significant under rib convection. (e) Normalised Y-direction oxygen concentration coloured by averaged velocity in the thickness of the GDL at each location. (For interpretation of the references to color in this figure legend, the reader is referred to the Web version of this article.)

Fig. 10 (a - b) show that oxygen is distributed more homogeneously and effectively in the cell, with enhanced diffusive and convective flux to the edges of the cell. There are some regions in the carbon paper material which are diffusion limited (blue regions at 0.23 mol m^{-3}) whereas in the 3D printed material, oxygen concentration remains high in those regions (green at 4 mol m^{-3}). Taking the oxygen concentration distribution data in the GDL region and averaging along the X-direction from the inlet to the outlet (Y-direction) produced the results in Fig. 10 (c). This shows that at all regions in the cell, the oxygen concentration in the cell is higher in the 3D printed material (green line) than the carbon paper material (black line). Furthermore, this shows that the 3D printed material is able to handle counter-flow transport better (from 0 to 0.0025 m) compared to the carbon paper material.

The improved diffusive and convective flux from the 3D structure can be seen in the visualisations of mass flux in Fig. 10 (d) where the flow is more homogeneous, and regions of low velocity are not found as frequently as in the carbon paper material. In both materials, in the current lab scale set up there is significant amount of convection in the under rib regions, this cross-flow is caused by the high pressure difference between the channels and is shown by the orange colours in Fig. 10 (d). These regions appear to be correlated to areas of greater oxygen transport, which can be seen in Fig. 10 (b) and (e − f). Where there is greater mass flux in the GDL, there is a greater concentration of oxygen at the catalyst layer surface as shown by the normalised y slice concentrations of oxygen shown in Fig. 10 (e − f). This clearly highlights the importance of in-plane permeability and convection which directly improves the advective transport of oxygen (shown by the more red colours associated with high velocity having the highest supply of oxygen at the catalyst surface).

The simulation results highlight that convection plays a key role in the mass transport capability of the GDL. While this study only looked at two cases in single-phase, the addition of liquid water will cause a significant divergence of results, where the 3D printed material should handle water management better and interfere with the oxygen transport less. To summarise, due to the higher permeability of the 3D printed material, the pressure drop in the cell was 27 Pa (compared to 54 Pa in the commercial material) and the average oxygen concentration at the CL was 8% higher than the carbon paper microstructure, which is promising, considering the thickness of the 3D printed structure is more than doubled.

Conclusion

For the first time, a designed 3D printed gas diffusion layer was used to replace a commercial carbon paper material used conventionally in the cathode of a PEMFC. The 3D printed design was successfully manufactured using a desktop UV printer, with a minimum pore size of 300 μm and minimum fibre size of 250 μm and with the macroscale dimensions of 0.8 × 50 × 50 mm. After optimising the carbonisation process by considering the thermogravimetric analysis of the cured resin, the structures were successfully carbonised at 900 °C under nitrogen atmosphere. Minimal

structural damage was incurred and electrical conductivity of around 180 S m^{-1} was exhibited. The structure wettability was altered with the addition of 5% wt PTFE and integrated into a lab scale fuel cell testing setup by spraying the MPL and CL onto the structure and subsequent hot-pressing to the membrane to form an MEA.

The electrochemical testing results show a lower power density than the commercial material. However, further analyses of the material using SEM, EIS, EDS and LSV have highlighted the reasons for this reduction. Firstly, membrane damage was caused by an uneven CL surface and large pore sizes, which allowed for significant hydrogen crossover and consequently a reduction in the OCV. Secondly, the distribution of the CL (e.g. around the fibres) did not form a flat surface; the contact area was effectively reduced by 54% and therefore contact resistances are introduced. Furthermore, the method of MPL/CL application (spray drying) allowed the MPL/CL agglomerated structure to penetrate the structure internally, both lowering the effective usage of catalytic active areas and altering the in-plane pore space resistance for oxygen transport.

The transient variations in cell performance highlighted the stability of the 3D printed electrode to deal with water management at the same current density; either by water vapour transport or liquid water removal. This is promising for commercialisation as less water flooding was observed; if the challenges with the implementation can be addressed, efficiency and durability gains should follow.

Using CFD simulations of the lab scale fuel cell cathode in both a carbon paper and 3D printed material structure, it was also shown that the effective oxygen distribution in the 3D material should be improved, if the challenges associated with cell engineering can be addressed.

As the first of its kind study, further research in material implementation and development will increase the OCV and allow a fairer comparison between a 3D printed electrode and the commercial material. To improve the performance of the 3D printed GDL, several challenges encountered in this study must be addressed. The first challenge would be to reduce membrane damage and subsequent hydrogen crossover, which could be addressed by reducing the pore scale accuracy of the 3D printer which would allow a smooth CL surface to be formed but also act to reduce membrane deformation into the pores. This could be achieved through an intermediate fine mesh structure on the bottom of the 3D printed material or by printing a joined GDL and microporous layer. The uneven catalyst distribution can be addressed by using a catalyst coated layer applied to the membrane. The electrical conductivity of the GDL could be increased further by using a furnace at higher operating temperatures, from 900 °C to around 2000 °C. The pyrolysis process could be optimised further to reduce processing time and material deformation.

Declaration of competing interest

The authors declare that they have no known competing financial interests or personal relationships that could have appeared to influence the work reported in this paper.

Acknowledgments

Appendix A. Supplementary data

Supplementary data to this article can be found online at https://doi.org/10.1016/j.ijhydene.2022.05.134.

REFERENCES

[1] Davis SJ, Lewis NS, Shaner M, Aggarwal S, Arent D, Azevedo IL, et al. Net-zero emissions energy systems. Science 2018;360.

[2] Guo Z, Chen J, Byun JJ, Perez—Page M, Ji Z, Zhao Z, et al. Insights into the performance and degradation of polybenzimidazole/muscovite composite membranes in high—temperature proton exchange membrane fuel cells. J Membr Sci 2022;641:1.

[3] Niblett D, Holmes SM, Niasar V. Discrete-particle model to optimize operational conditions of proton-exchange membrane fuel-cell gas channels. ACS Appl Energy Mater 2021;10(4):10514—33.

[4] Weber AZ, Borup RL, Darling RM, Das PK, Dursch TJ, Gu W, et al. A critical review of modeling transport phenomena in polymer-electrolyte fuel cells. J Electrochem Soc 2014;161:F1254—99.

[5] Gostick JT, Ioannidis MA, Fowler MW, Pritzker MD. Pore network modeling of fibrous gas diffusion layers for polymer electrolyte membrane fuel cells. J Power Sources 2007;173:277—90.

[6] Suresh PV, Jayanti S. Peclet number analysis of cross-flow in porous gas diffusion layer of polymer electrolyte membrane fuel cell (pemfc). Environ Sci Pollut Control Ser 2016;23:20 120—20 130. https://doi.org/10.1007/s11356-016-6629-x [Online]. Available:.

[7] Sim J, Kang M, Min K, Lee E, Jyoung J-Y. Effect of capillary pressure gradient in microporous layer on proton exchange membrane fuel cell performance. Int J Hydrogen Energy 2022;4 [Online]. Available: https://linkinghub.elsevier.com/retrieve/pii/S036031992201415X.

[8] Niblett D, Joekar-Niasar V, Holmes S. Enhancing the performance of fuel cell gas diffusion layers using ordered microstructural design. J Electrochem Soc 2018;167:13520.

[9] Niblett D, Mularczyk A, Niasar V, Eller J, Holmes S. Two-phase flow dynamics in a gas diffusion layer - gas channel - microporous layer system. J Power Sources 2020;471:228427. https://doi.org/10.1016/j.jpowsour.2020.228427 [Online]. Available:.

[10] Chen Q, Niu Z, Li H, Jiao K, Wang Y. Recent progress of gas diffusion layer in proton exchange membrane fuel cell: two-phase flow and material properties. 2021. p. 8640—71. 2.

[11] Csoklich C, Steim R, Marone F, Schmidt TJ, Buchi FN. Gas diffusion layers with deterministic structure for high performance polymer electrolyte fuel cells. ACS Appl Mater Interfaces 2021;13:9908—18. 3.

[12] Forner-Cuenca A, Biesdorf J, Gubler L, Kristiansen PM, Schmidt TJ, Boillat P. Engineered water highways in fuel cells: radiation grafting of gas diffusion layers. Adv Mater 2015;27:6317—22. 11.

[13] Jayakumar A, Singamneni S, Ramos M, Al-Jumaily AM, Pethaiah SS. Manufacturing the gas diffusion layer for pem fuel cell using a novel 3d printing technique and critical assessment of the challenges encountered. Materials 2017;10. 7.

[14] Guo L, Chen L, Zhang R, Peng M, Tao W-Q. Pore-scale simulation of two-phase flow and oxygen reactive transport in gas diffusion layer of proton exchange membrane fuel cells: effects of nonuniform wettability and porosity. 8 Energy 2022;253:124101 [Online]. Available: https://linkinghub.elsevier.com/retrieve/pii/S0360544222010040.

[15] Jervis R, Kok MD, Montagut J, Gostick JT, Brett DJ, Shearing PR. X-ray nano computed tomography of electrospun fibrous mats as flow battery electrodes. Energy Technol 2018;6:2488—500.

[16] Wen Y, Kok MD, Tafoya JPV, Sobrido ABJ, Bell E, Gostick JT, et al. Electrospinning as a route to advanced carbon fibre materials for selected low-temperature electrochemical devices: a review. J Energy Chem 2021;59:492—529 [Online]. Available: https://www.sciencedirect.com/science/article/pii/S2095495620307646.

[17] Pantò F, Fan Y, Stelitano S, Fazio E, Patanè S, Frontera P, et al. Electrospun c/geo2 paper-like electrodes for flexible li-ion batteries. Int J Hydrogen Energy 2017;42:28 102—128 112. 11.

[18] Sokka A, Mooste M, Käärik M, Gudkova V, Kozlova J, Kikas A, et al. Iron and cobalt containing electrospun carbon nanofibre-based cathode catalysts for anion exchange membrane fuel cell. Int J Hydrogen Energy 2021;46(61):31275—87.

[19] Yang Y, Zhou X, Tang F, Li B, Ming P, Zhang C. Failure behavior of gas diffusion layer in proton exchange membrane fuel cells. J Power Sources 2021;515. 12.

[20] Greer JR, Deshpande VS. Three-dimensional architected materials and structures: design, fabrication, and mechanical behavior. MRS Bull 2019;44:750—7. 10.

[21] Yan WM, Hsueh CY, Soong CY, Chen F, Cheng CH, Mei SC. Effects of fabrication processes and material parameters of gdl on cell performance of pem fuel cell. Int J Hydrogen Energy 2007;32:4452—8. 12.

[22] Santoro C, Agrios A, Pasaogullari U, Li B. Effects of gas diffusion layer (gdl) and micro porous layer (mpl) on cathode performance in microbial fuel cells (mfcs). Int J Hydrogen Energy 2011;36(20):13096—104.

[23] Yue L, Wang S, Araki T, Utaka Y, Wang Y. Effect of water distribution in gas diffusion layer on proton exchange membrane fuel cell performance. Int J Hydrogen Energy 2021;46:2969—77. 1.

[24] Shojaei MJ, Bijeljic B, Zhang Y, Blunt MJ. Minimal surfaces in porous materials: X-ray image-based measurement of the contact angle and curvature in gas diffusion layers to design optimal performance of fuel cells. 4 ACS Appl Energy Mater 2022;5:4613—21 [Online]. Available: https://pubs.acs.org/doi/10.1021/acsaem.2c00023.

[25] Behrou R, Pizzolato A, Forner-Cuenca A. Topology optimization as a powerful tool to design advanced pemfcs flow fields. Int J Heat Mass Tran 2019;135:72—92. 6.

[26] Wang X, Ma H, Peng H, Wang Y, Wang G, Xiao L, et al. Enhanced mass transport and water management of polymer electrolyte fuel cells via 3-d printed architectures. J Power Sources 2021;515. 12.

[27] Truong VM, Duong NB, Yang H. Effect of gas diffusion layer thickness on the performance of anion exchange membrane fuel cells. Processes 2021;9:4.

[28] Bian B, Shi D, Cai X, Hu M, Guo Q, Zhang C, et al. 3d printed porous carbon anode for enhanced power generation in microbial fuel cell. Nano Energy 2018;44:174—80. 2.

[29] Bian B, Wang C, Hu M, Yang Z, Cai X, Shi D, et al. Application of 3d printed porous copper anode in microbial fuel cells. Front Energy Res 2018;6. 6.

[30] Forner-Cuenca A, Brushett FR. Engineering porous electrodes for next-generation redox flow batteries: recent progress and opportunities. Current Opinion in Electrochemistry 2019;18:113—22. 12.

[31] Narita K, Citrin MA, Yang H, Xia X, Greer JR. 3d architected carbon electrodes for energy storage. Adv Energy Mater 2021;11. 2.

[32] Dudukovic NA, Fong EJ, Gemeda HB, DeOtte JR, Cerón MR, Moran BD, et al. Cellular fluidics. Nature 2021;595:58—65. 7.

[33] Lin J-H, Chen W-H, Su Y-J, Ko T-H. Effect of gas diffusion layer compression on the performance in a proton exchange membrane fuel cell. Fuel 2008;87(12):2420—4 [Online]. Available: https://www.sciencedirect.com/science/article/pii/S0016236108000999.

[34] Kulkarni N, Cho JI, Jervis R, Roberts EP, Francesco I, Kok MD, et al. The effect of non-uniform compression on the performance of polymer electrolyte fuel cells. J Power Sources 2022;521:230973 [Online]. Available: https://www.sciencedirect.com/science/article/pii/S0378775321014567.

[35] Singh Y, White RT, Najm M, Boswell A, Orfino FP, Dutta M, et al. Mitigation of mechanical membrane degradation in fuel cells by controlling electrode morphology: a 4d in situ structural characterization. J Electrochem Soc 2021;168:34521. 3.

[36] Zhang X, Vyatskikh A, Gao H, Greer JR, Li X. Lightweight, flaw-tolerant, and ultrastrong nanoarchitected carbon. Proc Natl Acad Sci U S A 2019;116:6665—72. 4.

[37] Bauer J, Schroer A, Schwaiger R, Kraft O. Approaching theoretical strength in glassy carbon nanolattices. Nat Mater 2016;15:438—43. 4.

[38] Ruiz-Morales JC, Tarancón A, Canales-Vázquez J, Méndez-Ramos J, Hernández-Afonso L, Acosta-Mora P, et al. Three dimensional printing of components and functional devices for energy and environmental applications. Energy & Environmental Science 2017:846—59. 4.

[39] Pesce A, Hornés A, Núñez M, Morata A, Torrell M, Tarancón A. 3d printing the next generation of enhanced solid oxide fuel and electrolysis cells. J Mater Chem 2020;8(33):16926—32.

[40] Islam M, Lantada AD, Gómez MR, Mager D, Korvink JG. Microarchitectured carbon structures as innovative tissue-engineering scaffolds. Adv Eng Mater 2020;22. 6.

[41] Portela CM, Edwards BW, Veysset D, Sun Y, Nelson KA, Kochmann DM, et al. Supersonic impact resilience of nanoarchitected carbon. Nat Mater 2021;20:1491—7. 11.

[42] Sharma S. Glassy carbon: a promising material for microand nanomanufacturing. Materials 2018;11.

[43] Rai AA, Yanilmaz M. High-performance nanostructured bio-based carbon electrodes for energy storage applications. Cellulose 2021:5169—218. 6.

[44] Mondal M, Goswami DK, Bhattacharyya TK. Lignocellulose based bio-waste materials derived activated porous carbon as superior electrode materials for high-performance supercapacitor. J Energy Storage 2021;34. 2.

[45] Arun S, Kiran KUV, Kumar SM, Karnan M, Sathish M, Mayavan S. Effect of orange peel derived activated carbon as a negative additive for lead-acid battery under high rate discharge condition. J Energy Storage 2021;34. 2.

[46] Zhang G, Chen Y, Chen Y, Guo H. Activated biomass carbon made from bamboo as electrode material for supercapacitors. Mater Res Bull 2018;102:391—8. 6.

[47] Krzesińska M. Anisotropy of skeleton structure of highly porous carbonized bamboo and yucca related to the pyrolysis temperature of the precursors. J Anal Appl Pyrol 2017;123:73—82. 1.

[48] Krzesińska M, Pilawa B, Pusz S, Ng J. Physical characteristics of carbon materials derived from pyrolysed vascular plants. Biomass Bioenergy 2006;30:166—76. 2.

[49] Kunowsky M, Weinberger B, Darkrim FL, Suárez-García F, Cazorla-Amorós D, Linares-Solano A. Impact of the carbonisation temperature on the activation of carbon fibres and their application for hydrogen storage. Int J Hydrogen Energy 2008;33:3091—5. 6.

[50] Rezaei B, Pan JY, Gundlach C, Keller SS. Highly structured 3d pyrolytic carbon electrodes derived from additive manufacturing technology. Mater Des 2020;193:108834 [Online]. Available: https://www.sciencedirect.com/science/article/pii/S0264127520303683.

[51] Dehghanpour H, Yilmaz K. The relationship between resistances measured by two-probe, wenner probe and c1760-12 astm methods in electrically conductive concretes. SN Appl Sci 2020;2:1.

[52] Hosseinpour M, Sahoo M, Perez-Page M, Baylis SR, Patel F, Holmes SM. Improving the performance of direct methanol fuel cells by implementing multilayer membranes blended with cellulose nanocrystals. Int J Hydrogen Energy 2019;44:30409—430 419. 11.

[53] Ji Z, Perez-Page M, Chen J, Rodriguez RG, Cai R, Haigh SJ, et al. A structured catalyst support combining electrochemically exfoliated graphene oxide and carbon black for enhanced performance and durability in low-temperature hydrogen fuel cells. Energy 2021;226:7.

[54] Herrera C, Sierra-Pérez J, Nieto-Londoño C. Analytical determination of viscous permeability of hybrid fibrous reinforcements. Int J Thermofluids 2020;7—8:100042 [Online]. Available: https://www.sciencedirect.com/science/article/pii/S266620272030029X.

[55] Hwang GS, Weber AZ. Effective-diffusivity measurement of partially-saturated fuel-cell gas-diffusion layers. J Electrochem Soc 2012;159:F683—92 [pTFE treatment favorably changes liquid distribution for improved gas transport pathways].

[56] Das PK, Grippin A, Kwong A, Weber AZ. Liquid-water-droplet adhesion-force measurements on fresh and aged fuel-cell gas-diffusion layers. J Electrochem Soc 2012;159(5):B489—96. https://doi.org/10.1149/2.052205jes [Online]. Available:.

[57] Daicho Y, Murakami T, Hagiwara T, Maruo S. Formation of three-dimensional carbon microstructures via two-photon microfabrication and microtransfer molding. Opt Mater Express 2013;3:875. 6.

[58] Schueller OJA, Brittain ST, Whitesides GM. Fabrication of glassy carbon microstructures by pyrolysis of microfabricated polymeric precursors. Advanced Materials Communications 1996;167:477—80.

[59] Ramani JFV, Kunz HR. The chalkboard: the polymer electrolyte fuel cell. The Electrochemical Society Interface 2014;13:17.

[60] Dotelli G, Ferrero R, Stampino PG, Latorrata S. Analysis and compensation of pem fuel cell instabilities in low-frequency eis measurements. IEEE Trans Instrum Meas 2014;63:1693—700.

[61] Andreasen SJ, Jespersen JL, Schaltz E, Kær SK. Characterisation and modelling of a high temperature pem fuel cell stack using electrochemical impedance spectroscopy. Fuel Cells 2009;9(8):463—73.